NANO LETTERS

Letter

pubs.acs.org/NanoLett

Microwave Near-Field Imaging of Two-Dimensional Semiconductors

Samuel Berweger,*[,†] Joel C. Weber,[†] Jimmy John,[§] Jesus M. Velazquez,[‡,§] Adam Pieterick,[‡,§] Norman A. Sanford,[†] Albert V. Davydov,[∥] Bruce Brunschwig,[‡,§] Nathan S. Lewis,[‡,§] Thomas M. Wallis,[†] and Pavel Kabos[†]

[†]National Institute of Standards and Technology, Boulder, Colorado 80305, United States

[‡]Kavli Nanoscience Institute, Beckman Institute, Joint Center for Artificial Photosynthesis and [§]Division of Chemistry and Chemical Engineering, California Institute of Technology, Pasadena, California 91125, United States

[∥]National Institute of Standards and Technology, Gaithersburg, Maryland 20899, United States

Supporting Information

ABSTRACT: Optimizing new generations of two-dimensional devices based on van der Waals materials will require techniques capable of measuring variations in electronic properties in situ and with nanometer spatial resolution. We perform scanning microwave microscopy (SMM) imaging of single layers of MoS_2 and n- and p-doped WSe_2. By controlling the sample charge carrier concentration through the applied tip bias, we are able to reversibly control and optimize the SMM contrast to image variations in electronic structure and the localized effects of surface contaminants. By further performing tip bias-dependent point spectroscopy together with finite element simulations, we distinguish the effects of the quantum capacitance and determine the local dominant charge carrier species and dopant concentration. These results underscore the capability of SMM for the study of 2D materials to image, identify, and study electronic defects.

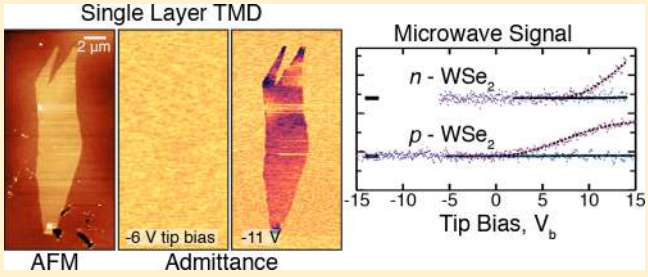

KEYWORDS: *Transition metal dichalcogenide, MoS_2, microwave, near-field, quantum capacitance, atomic force microscope*

Two-dimensional (2D) materials have emerged as a source of novel fundamental physics[1,2] and are expected to form building blocks for hybrid materials with stacking-dependent tunable properties. While the palette of suitable materials is rapidly expanding,[3] the semiconducting transition metal dichalcogenides (TMDs) have emerged as promising materials for applications ranging from catalysis[4] to electronic devices.[5−9] In particular, TMD-based van der Waals heterostructure analogues of traditional semiconducting devices are rapidly being demonstrated and improved.[10,11] However, with device fabrication still imprecise, resulting performance is often highly variable due to sample-dependent differences in electronic properties that arise from doping and associated spatial inhomogeneities such as structural defects.

In order to understand variations between devices as they relate to their performance, techniques to identify and study the electronic inhomogeneities in 2D semiconductor materials in situ and on their characteristic nanometer length scales are highly desirable. While electron-based techniques such as transmission electron microscopy are well suited to study the structural defects that underlie many electronic discontinuities,[12] they are time-consuming and require specialized sample preparation. In contrast, scanning probe techniques can obtain simultaneous topographic and electronic information with nanometer spatial resolution, are nondestructive, and can operate under ambient conditions with little sample preparation. However, some common scanning probe implementations such as scanning gate microscopy[13] require fabricated electrodes to achieve a transistor-like geometry, which often alters material properties. While scanning capacitance microscopy[14] does not require electrodes, material information is lost as it typically measures only the imaginary (capacitive) portion of the complex-valued sample impedance, and the overall signal strength is reduced due to the lower (typically on the order of MHz) frequencies used.

In scanning microwave microscopy (SMM),[15] a gigahertz (GHz) signal applied to a scanning probe tip measures the complete complex-valued tip−sample admittance $\tilde{Y}$ resulting from the local electronic properties. Contact electrodes are not required and insulating or electrically isolated samples can readily be measured. While SMM is capable of quantitative capacitance determination in dedicated sample architectures,[16] applications to solid-state systems typically yield qualitative conductivity measurements,[17] and studies of 2D materials have largely focused on graphene.[18−21] SMM imaging of the prototypical TMD MoS_2 was able to resolve the presence of growth defects and grain boundaries via conductivity changes but the single TMD layer itself showed only weak contrast and the electronic origin of these effects was not established.[19]

Received: October 24, 2014
Revised: January 20, 2015
Published: January 27, 2015

ACS Publications © 2015 American Chemical Society

DOI: 10.1021/nl504960u
Nano Lett. 2015, 15, 1122−1127

Here we demonstrate a new approach to SMM imaging of 2D materials, which we illustrate with the TMDs MoS_2 and WSe_2. By controlling the TMD conductivity via the tip bias-dependent charge carrier concentration, we significantly improve the otherwise poor contrast from single-layer crystals and identify spatial inhomogeneities in electronic structure. For single-layer systems, we further perform tip bias-dependent point spectroscopy, which we combine with finite element simulations and simple band structure approximations to extract doping concentrations and the associated quantum capacitance, which is in good agreement with expected values. Within thicker crystals, large variations in electronic properties are seen, revealing a complex behavior resulting from thickness dependent doping, the band structure, and possible interactions between layers of different thicknesses. While we use TMDs as model systems, this method is in principle applicable to all semiconducting van der Waals materials and heterostructures.

MoS_2 samples were obtained commercially (SPI supplies) while stochiometric WSe_2 (n-doped) and $W_{1-x}Nb_xSe_2$ ($x \approx 0.01$, heavily p-doped) were grown by chemical vapor transport.[22] Substrates were prepared by growing 260 nm of thermal oxide on p^{+2}-doped Si for optimal visibility of TMDs,[23] followed by solvent cleaning and O_2 plasma ash to remove residual organics. TMD crystals were prepared by conventional micromechanical exfoliation.[24] Few-layer regions were identified by optical microscopy and studied under ambient conditions. Figure 1a shows an optical image of a MoS_2 sheet with superimposed contact mode atomic force microscope (AFM) topography confirming single-layer thickness of ~0.7 nm.

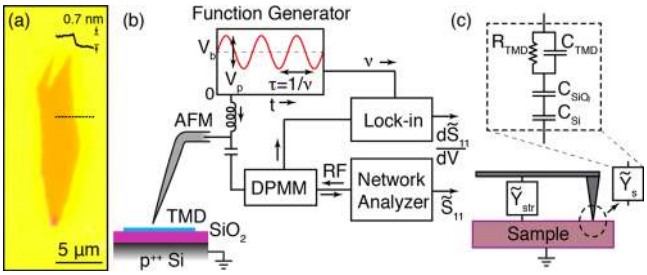

Figure 1. (a) Optical image of single-layer MoS_2 exfoliated onto SiO_2/Si. Inset: AFM topographic line cut along dashed line confirming single-layer thickness. (b) Experimental schematic of SMM setup with simultaneous detection of $\tilde{S}_{11}$ and $\tilde{S}'_{11} = d\tilde{S}_{11}/dV$ signals. (c) Lumped element model with cantilever-sample stray admittance $\tilde{Y}_{str}$ and sample admittance $\tilde{Y}_s$.

The SMM is based on a commercial AFM (Agilent 5400) operating in SMM mode as illustrated in Figure 1b. The microwave signal delivered to the tip is sourced from a vector network analyzer, which also detects the reflected signal, $\tilde{S}_{11}$. A dc bias V_b and low-frequency signal V_p with a combined maximum of ~± 15 V are summed with the microwave signal at the tip. By modulating V_p at a frequency ν = 15 kHz and V_p = 2 V, together with a dopant profiling measurement module (DPMM)[25] and lock-in detection, we measure the differential signal $d\tilde{S}_{11}/dV = \tilde{S}'_{11}$ concurrently with $\tilde{S}_{11}$. Raster-scanned images are acquired with a lock-in time constant τ = 10 ms, while $\tilde{S}'_{11}$-voltage sweeps use longer acquisition times $\tau \geq 100$ ms for improved sensitivity.

In order to maintain electrical contact to the TMD sheets and minimize adverse effects on experimental sensitivity from the stray admittance $\tilde{Y}_{str}$, as shown in Figure 1c we use 80 μm tall platinum cantilevers (Rocky Mountain Nanotechnology) in contact mode feedback. However, we find the $\tilde{S}_{11}$ signal to be highly sensitive to ambient effects and as a result use the robust $\tilde{S}'_{11}$ signal (see Supporting Information).

Shown in Figure 2a is the contact mode AFM topography of an exfoliated WSe_2 patch with single and three-layer regions as indicated. The large center portion of the patch has a terraced structure with varying thickness, as well as a large region near the top with poor substrate adhesion. The $\tilde{S}'_{11}$ signal is acquired simultaneously with the topography at a frequency of ν = 2.39 GHz, and after correcting for the stray admittance gives $\tilde{S}' \propto \tilde{Y}'_{TMD}$ (see Supporting Information). Also shown in Figure 2 are $S'_R = \mathrm{Re}(\tilde{S}')$ (b) and $S'_C = \mathrm{Im}(\tilde{S}')$ (c), the resistive and capacitive signal components, respectively. While neither signal component shows any visible contrast from the WSe_2 patch at zero tip bias, S'_R increases strongly with tip bias while a smaller increase is seen in S'_C. Overall the contrast is stronger over the bulklike thicker regions with changes in contrast between layers mostly seen in S'_R. Compared to the thicker regions, contrast from the three-layer region emerges only at higher bias and the single-layer remains without discernible contrast during imaging.

We find that all TMD materials studied here follow a qualitatively similar tip bias dependence of the signal. Shown in Figure 3 are AFM topography (i) and SMM images (ii–v) acquired from single and bilayer $W_{1-x}Nb_xSe_2$ (a) and single-layer MoS_2 (b). Both materials show little or no signal under neutral bias, but it increases at positive biases for $W_{1-x}Nb_xSe_2$ and negative biases for MoS_2, notably improving visibility of sheets. Little or no contrast is seen in S'_C in all cases as further discussed below. Furthermore, no signal is seen at negative bias

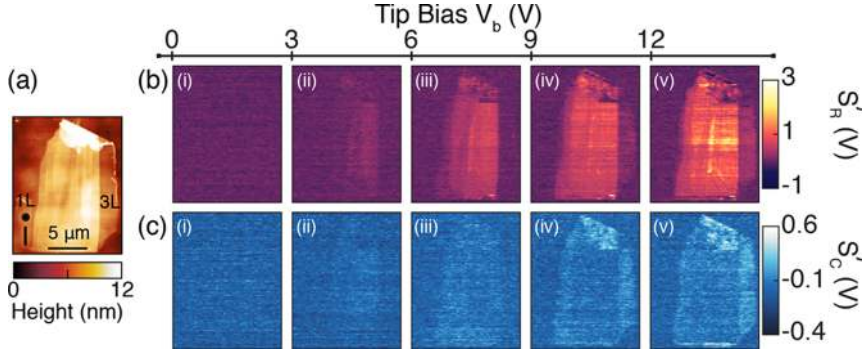

Figure 2. (a) AFM topography of an exfoliated patch of WSe_2 with few-layer regions as indicated. Sequence of S'_R (b) and S'_C (c) scans with tip bias as indicated.

DOI: 10.1021/nl504960u
Nano Lett. 2015, 15, 1122–1127

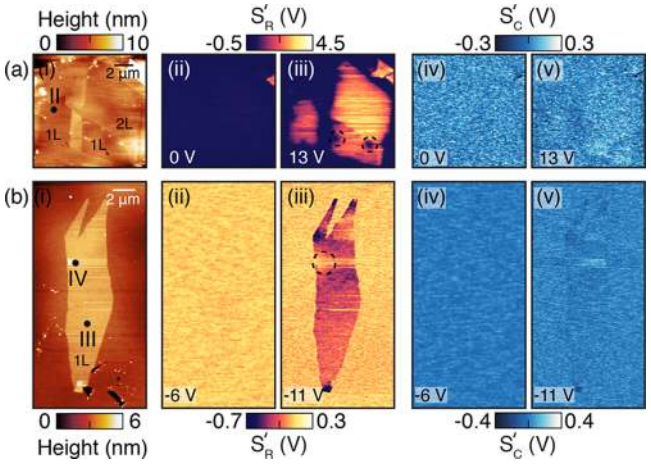

Figure 3. AFM topography (i) and SMM images (ii–v) of few layer $W_{1-x}Nb_xSe_2$ (a) and single-layer MoS_2 (b) with tip bias V_b as indicated. Note decreased pixel density in (b,ii) and (b,iv).

for both species of WSe_2 and for positive bias for MoS_2 with the same trend observed in $\tilde{S}_{11}$ (not shown). For all materials, signal variations are seen within single sheets both over distances of several microns, as well as locally due to surface defects, with examples illustrated by dashed circles.

Some line-to-line signal variations are seen. This arises from increases in the tip–sample resistance due to, for example, residual soft matter from exfoliation adsorbing onto the tip and is often seen from large surface defects. However, signal levels quickly return to expected values and scans are highly reproducible (see Supporting Information), suggesting that the tip–sample contact is robust and that adsorbates do not accumulate and are rapidly removed during scanning due to the tip–sample friction.

In order to understand the origin of the observed contrast we model our system using finite-element solving software (COMSOL 4.2). Shown in Figure 4a is the model axisymmetric

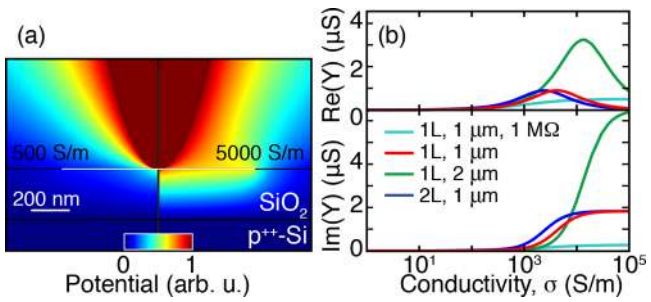

Figure 4. (a) Geometry used for finite element simulations. Left and right panels show spatial distribution of the calculated quasistatic potential for two different TMD sheet conductivities as indicated. (b) Conductivity-dependent admittance for TMD geometry with thickness and sheet diameter as indicated. Contact resistance is 50 Ω unless otherwise noted.

geometry[26] with a single-layer TMD shown in white. The TMD thickness of 0.65 nm is based on accepted values[5] to maximize the accuracy of our simulations. The left and right panel show the spatial distribution of the quasistatic potential for two different single-layer TMD sheets with in-plane dielectric constant $\varepsilon = 7$[27] and conductivities as indicated (see Supporting Information for further details). Figure 4b shows the calculated conductivity-dependent admittance $\tilde{Y}_{TMD} = (1/R_{TMD}) + i\omega C_{geo}$ with the geometric capacitance $C_{geo} = C_{TMD}$ for sheet thicknesses and diameter as indicated. The resonance-type behavior in Figure 4b shifts to lower conductivity for thicker sheets and to higher values with larger admittances for larger TMD sheets.[18] While qualitatively the same, quantitative differences to similar calculations[18−20,26] are primarily due to the imposition of a 50 Ω conductive tip-TMD contact here. An increased contact resistance of 1 MΩ leads to notable changes in the conductivity-dependent contrast as shown in Figure 4b with typical variations in resistance estimated to be ≤100 kΩ (see Supporting Information).

The observed tip bias-dependent contrast is thus attributed to changes in TMD conductivity. As further discussed below, the tip-TMD contact allows charge to flow, thereby changing the carrier concentration n in the semiconductor and associated conductivity $\sigma = ne\mu$ with elementary charge e and carrier mobility μ. Under ambient experimental conditions, both MoS_2 and WSe_2 show strong unipolar charge transport behavior with clear n-type transport[6] and p-type transport,[28] respectively. With large differences in hole and electron mobilities at room temperature,[28] only the dominant charge carrier for each species results in conductivities sufficiently large to produce a measurable SMM signal over the voltage range studied here. As a consequence, a positive (negative) tip bias increases the hole (electron) density in WSe_2 (MoS_2), thereby increasing the conductivity as seen in Figures 2 and 3.

To simulate the measured S'-voltage behavior we fit our simulation results to bias-dependent data using a phenomenological approach. To approximate the relationship between charge carrier density and V_b we use the integrated density of states (DOS) at the band edge. We assume a quadratic band-edge DOS in good approximation to theoretical results for an energy range of ∼1 eV.[29−32] We thus have $(dn_i/dE) \propto |E - E_{b,i}|^2$ with $(i = e^-, h^+)$ and the band edge energy $E_{b,i}$. By integrating we find $n_e \propto -(aV_b - E_0)^3 = \sigma_{MoS_2}$ and $n_e \propto (aV_b - E_0)^3 = \sigma_{WSe_2}$, where the constant a reflects the scaling relationship between E and V_b, and E_0 accounts for doping at 0 bias (i.e., Fermi level shift).

S'-voltage point spectroscopy was performed on single-layer regions for all TMD materials studied here in order to further investigate the local electronic structure and the effects of local surface defects. Shown in Figure 5 are S'_R (a) and S'_C (b) acquired from locations (I–IV) as indicated in Figures 2 and 3 with (IV) taken from the vicinity of the electronic defect on MoS_2. Consistent with scan sequences, for the WSe_2 species the contrast increased with positive bias while for MoS_2 negative contrast increases for negative bias. Overall, S'_R is significantly larger than S'_C in part due to the increase of $\mathrm{Re}(\tilde{Y}(\sigma))$ at lower values of σ. Note that the onset of contrast is observed at lower values of V_b here compared to Figures 2 and 3 due to the significantly larger lock-in time constant used for sweeps. Solid lines in Figure 5a show the simulation fit to $\mathrm{Re}(\tilde{Y}'(V_b))$ with simulations repeated for each material to account for TMD sheet size. While excellent agreement is seen for the real component of the signal for all materials, the solid lines in Figure 5b show $\mathrm{Im}(\tilde{Y}'(V_b))$ using the same parameters where the simulated increase in the imaginary part is not seen.

The difference between the measured and calculated values of S'_C are attributed primarily to the quantum capacitance.[33,34] Because the quantum capacitance arises from the finite DOS of low-dimensional materials,[35] it is frequency-independent into

DOI: 10.1021/nl504960u
Nano Lett. 2015, 15, 1122−1127

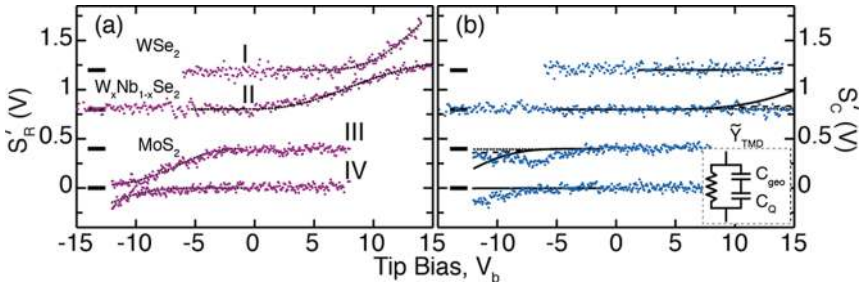

Figure 5. Resistive (a) and capacitive (b) components of S'-voltage sweeps taken from locations (i–iv) as shown in Figures 2 and 3. Black lines in (a) are fits to S'_R using finite element simulations. Solid and dashed lines in (b) are fits to S'_C with and without consideration of the quantum capacitance, respectively. Inset shows $\tilde{Y}_{TMD}$ with quantum capacitance C_Q in series with geometric capacitance C_{geo} Sweeps are offset for clarity.

the GHz range, and it appears in series with the geometric capacitance[33] as shown in the inset of Figure 5b. It is directly related to the voltage-dependent two-dimensional charge density Q by $C_Q = (dQ/dV)$. We estimate Q, and thus the quantum capacitance, from the bias-dependent conductivity obtained from the simulation fit and assuming ambient room temperature mobilities of $\mu = 10$ cm^2/V·s.[5,28] Shown in Figure 5b is the calculated Im($\tilde{Y}'(V_b)$) without quantum capacitance (solid lines) and with calculated quantum capacitance (dashed and dotted) by $C_{TMD}^{-1} = C_{geo}^{-1} + C_Q^{-1}$. The dashed and dotted lines assume a constant area with radii of 0.25 and 0.1 μm contributing to the quantum capacitance, respectively. Although the spatial extent of the effective area contributing to the capacitance is bias-dependent, an estimate based on the full width at half maximum of the spatial distribution of the simulated quasistatic potential suggests that this area is smaller than a disk of 0.25 μm for all values of the conductivity considered here. With $C_Q < C_{geo}$ for large values of the conductivity, the series capacitance is dominated by the smaller value and does not increase as calculated from the simulations alone. As a consequence, good agreement is seen with S'_C and S'_R for the case of WSe_2 and $W_{1-x}Nb_xSe_2$, although the increase in S'_C seen for MoS_2 suggests the influence of additional capacitive effects not accounted for here, including charges at the SiO_2–MoS_2 interface.

The fit parameters E_0 and a directly relate to material electronic properties. For the scaling parameter a we find $a \approx 1.1$ for both WSe_2 species and $a \approx 2$ for pristine MoS_2. This corresponds to the steeper increase in the calculated band edge integrated DOS for electrons than holes expected for TMDs[30−32] and supports our approximation.

E_0 is found to change with material according to doping levels and carrier type and for $V_b = 0$ can be used to estimate the charge carrier density via the corresponding values of σ. For the case of pristine MoS_2 and $W_{1-x}Nb_xSe_2$ with $E_0 = 2$ V and $E_0 = -4.5$ V, we estimate carrier concentrations of $n_e = 5 \times 10^{16}$ cm^{-3} and $n_p = 5 \times 10^{17}$ cm^{-3}, respectively, which is in good agreement with expected values.[5,22] For the case of WSe_2, the value $E_0 = 2$ V reflects the expected negative doping of the material, which requires carrier inversion in order for appreciable SMM signal to be obtained. Similarly, for the case of the MoS_2 defect, the value of $E_0 = -2$ V indicates modification of the local electronic structure via hole-doping, although the poor agreement for S'_C suggests additional electronic effects.

These results underscore the applicability of SMM for nondestructive characterization of 2D materials. Similar to previous results, in the absence of a tip bias our imaging shows little or no signal from single-layer[19] as well as thicker TMD sheets. However, by applying a tip bias to modify the sample conductivity and carrier type we can control and optimize the sample contrast in order to readily identify spatial variations in the $\tilde{S}'$ signal arising from electronic inhomogeneities as well as localized electronic defects. Using $\tilde{S}'$-voltage point spectroscopy we obtain excellent agreement between the measured and simulated tip bias-dependent signal for the real (resistive) data which we use to semiquantitatively determine carrier concentration and type. We further account for the quantum capacitance via the bias-dependent charge carrier concentration obtained form the simulation fit, which significantly improves agreement for the imaginary (capacitive) data. Although our calculated quantum capacitance on the order of 100 nF/cm^2 is significantly smaller than typical values for 2D materials of 1–10 μF/cm^2,[34,36] its value is highly dependent on the sample geometry.[37] In particular, with quantum capacitances typically measured in a transistor geometry through a gate oxide with typical thickness <5 nm, our measured quantum capacitance is expected to be significantly smaller[14] with the tip bias referenced against the Si ground through a 260 nm oxide layer. Although the quantum capacitance provides good agreement in S'_C for the WSe_2 species, differences for MoS_2 remain, likely arising due to interfacial charging and effects that will be the subject of future investigations.

Of particular interest is the nature of the tip–sample interaction, as there has been significant debate regarding the electronic nature of metal-TMD contacts.[38] We find that our signal is dominated by the resistive signal component, which strongly suggests a noncapacitive junction. Furthermore, a capacitively coupled MIS junction would be expected to yield $\tilde{S}'$-voltage curves based on intrinsic doping, characterized by contrast at opposite bias values for n- and p-doped WSe_2[39] (see Supporting Information), as observed in previous SMM studies.[25,40,41] We therefore conclude that our tip-TMD interaction results in a largely resistive junction. Our reproducible signal levels strongly suggest a low-resistance contact, which is consistent with reports that such contacts to TMDs are routinely established using high work function metals.[5,7] This underscores a unique advantage of 2D materials: unlike conventional semiconductors with dangling surface bonds, 2D material surfaces do not react under ambient conditions to form insulating oxide layers.

As the tip–sample junction readily allows charge to flow to the sample, we have assumed a uniform conductivity across the TMD sheet in response to the dc tip bias. For small values of the conductivity, however, high associated sheet resistances $\gtrsim$1 GΩ may prevent effective charge equilibration. As our signal onset is typically around $\sigma \approx 100$ S/m, we do not expect that resulting conductivity variations affect our measurements.

DOI: 10.1021/nl504960u
Nano Lett. 2015, 15, 1122–1127

Simulations of conductivity variations in the immediate vicinity of the tip suggest that the primary influence of such effects would be changes in our estimate of the zero-bias conductivity and doping (see Supporting Information).

While much of the interest in TMDs and van der Waals materials in general have focused on single-layer systems, multilayer systems also hold promise for technological applications.[8,9] For the single-layer $\tilde{S}'$-voltage sweeps shown here, the behavior is largely consistent among several single-layer regions studied, although some inhomogeneity is observed both within and between crystals. Unlike single layers, crystals thicker than two or three layers exhibit widely varying $\tilde{S}'$-voltage behavior as seen in Figure 2b. While the origin of this behavior is unclear, it likely originates from thickness-dependent doping,[42] together with the complexity of the DOS structure[30−32] not accounted for by the quadratic approximation used. These results caution that device applications based on multilayer TMD materials require uniform film thicknesses.

As optimal device performance of 2D materials necessitates uniform structural and electronic properties over a large region, the capability for in situ characterization of devices and sheets is highly desirable. Even within single sheets of TMD materials, a large degree of electronic inhomogeneity can be observed and locally measured. The measured electronic effects of the MoS_2 surface defect with the region influenced by the defect significantly larger than its physical size suggest this defect strongly p-dopes its immediate vicinity.

We have demonstrated that microwave near-field microscopy together with tip bias-dependent control of carrier concentration and associated spectroscopy can be used to optimize sample contrast as well as extract local doping values of both pristine sheets and defects. In this respect, SMM is a highly attractive technique, capable of studying the local electronic structure and its spatial variations with nanometer resolution without the need for electrode deposition or device modification. While providing useful information on its own, this technique should not be viewed as a stand-alone method. Rather, SMM is compatible with and can yield complementary information to other electrostatic and electrodynamic scanning probe techniques.[13,14] Although demonstrated for the specific case of TMD materials, this technique is in principle applicable to any 2D semiconducting system. Of particular interest are van der Waals heterojunctions where the tunability of material properties via interlayer interactions[30] combined with expected spatial variations in material properties will necessitate the spatially resolved determination of electronic structure.

■ ASSOCIATED CONTENT

Supporting Information

We provide a comparison of the S_{11} and S' signals, demonstrate the signal reproducibility, discuss the origin of the signal, provide additional details of the simulations, and show additional simulations exploring tip−sample contact resistance and varying sample conductivity. This material is available free of charge via the Internet at http://pubs.acs.org.

■ AUTHOR INFORMATION

Corresponding Author

*E-mail: samuel.berweger@nist.gov.

Notes

The authors declare no competing financial interest.

■ ACKNOWLEDGMENTS

We would like to thank Will Gannett, Mark Keller, and Alexandra Curtin for helpful advice on sample preparation. This material is based upon work performed by the Joint Center for Artificial Photosynthesis, a DOE Energy Innovation Hub, supported through the Office of Science of the U.S. Department of Energy under Award Number DE-SC0004993. Mention of commercial products is for informational purposes only, it does not imply NIST's recommendation or endorsement.

■ REFERENCES

(1) Mak, K. F.; Lee, C.; Hone, J.; Shan, J.; Heinz, T. F. *Phys. Rev. Lett.* **2010**, *105*, 136805.
(2) Geim, A. K.; Novoselov, K. S. *Nat. Mater.* **2007**, *6*, 183.
(3) Li, L.; Yu, Y.; Ye, G. J.; Ge, Q.; Ou, X.; Wu, H.; Feng, D.; Chen, X. H.; Zhang, Y. *Nat. Nanotechnol.* **2014**, *9*, 372.
(4) Velazquez, J. M.; Saadi, F. H.; Pieterick, A. P.; Spurgeon, J. M.; Soriaga, M. P.; Brunschwig, B. S.; Lewis, N. S. *J. Electronanal. Chem.* **2014**, *716*, 45.
(5) Radisavljevic, B.; Radenovic, A.; Brivio, J.; Giacometti, V.; Kis, A. *Nat. Nanotechnol.* **2011**, *6*, 147.
(6) Bao, W.; Cai, X.; Kim, D.; Sridhara, K.; Fuhrer, M. *Appl. Phys. Lett.* **2013**, *102*, 042104.
(7) Liu, W.; Kang, J.; Sakar, D.; Khatami, Y.; Jena, D.; Banerjee, K. *Nano Lett.* **2013**, *13*, 1983.
(8) Kim, S.; Konar, A.; Hwang, W. S.; Lee, K. H.; Lee, J.; Yang, J.; Jung, C.; Kim, H.; Yoo, J. B.; Choi, J. Y.; Jin, Y. W.; Lee, S. Y.; Jena, D.; Choi, W.; Kim, K. *Nature Commun.* **2012**, *3*, 1011.
(9) Ganatra, R.; Zhang, Q. *ACS Nano* **2014**, *8*, 4074.
(10) Lee, C. H.; Lee, G. H.; van der Zande, A. M.; Chen, W.; Li, Y.; Han, M.; Cui, X.; Arefe, G.; Nuckolls, C.; Heinz, T. F.; Guo, J.; Hone, J.; Kim, P. *Nat. Nanotechnol.* **2014**, *9*, 676.
(11) Ross, D. S.; Klement, P.; Jones, A. M.; Ghimire, N. J.; Yan, J.; Mandrus, D. G.; Taniguchi, T.; Watanabe, K.; Yao, W.; Cobden, D. H.; Xu, X. *Nat. Nanotechnol.* **2014**, *9*, 268.
(12) van der Zande, A. M.; Huang, P. Y.; Chenet, D. A.; Berkelbach, T. C.; Yu, Y. M.; Lee, G. H.; Heinz, T. F.; Reichmann, D. R.; Muller, D. A.; Hone, J. C. *Nat. Mater.* **2013**, *12*, 554.
(13) Connolly, M. R.; Puddy, R. K.; Logoteta, D.; Marconcini, P.; Roy, M.; Griffiths, J. P.; Jones, G. A. C.; Maksym, P. A.; Macucci, M.; Smith, C. G. *Nano Lett.* **2012**, *12*, 5448.
(14) Giannazzo, F.; Sonde, S.; Raineri, V.; Rimini, E. *Nano Lett.* **2009**, *9*, 23.
(15) Fee, M.; Chu, S.; Hänsch, T. W. *Opt. Commun.* **1989**, *69*, 219.
(16) Huber, H. P.; Moertelmaier, M.; Wallis, T. M.; Chiang, C. J.; Hochleitner, M.; Imtiaz, A.; Oh, Y. J.; Schilcher, K.; Dieudonne, M.; Smoliner, J.; Hinterdorfer, P.; Rosner, S. J.; Tanbakuchi, H.; Kabos, P.; Kienberger, F. *Rev. Sci. Instrum.* **2010**, *81*, 113701.
(17) Lai, K.; Nakamura, M.; Kundhikanjana, W.; Kawasaki, M.; Tokura, Y.; Kelly, M. A.; Shen, Z. X. *Science* **2010**, *239*, 190.
(18) Kundhikanjana, W.; Lai, K.; Wang, H.; Dai, H.; Kelly, M. A.; Shen, Z. X. *Nano Lett.* **2009**, *9*, 3762.
(19) Liu, Y.; Ghosh, R.; Wu, D.; Ismach, A.; Ruoff, R.; Lai, K. *Nano Lett.* **2014**, *14*, 4682.
(20) Tselev, A.; Lavrik, N. V.; Vlassiouk, I.; Briggs, D. P.; Rutgers, M.; Proksch, R.; Kalinin, S. V. *Nanotechnology* **2012**, *23*, 385706.
(21) Talanov, V. V.; Del Barga, C.; Wickey, L.; Kalichava, I.; Gonzales, E.; Shaner, E. A.; Gin, A. V.; Kalugin, N. G. *ACS Nano* **2010**, *4*, 3831.
(22) McKone, J. R.; Pieterick, A. P.; Gray, H. B.; Lewis, N. S. *J. Am. Chem. Soc.* **2013**, *135*, 223.
(23) Benameur, M. M.; Radisavljevic, B.; Héron, J. S.; Sahoo, S.; Berger, H.; Kis, A. *Nanotechnology* **2011**, *22*, 125706.
(24) Novoselov, K. S.; Jiang, D.; Schedin, F.; Booth, T. J.; Khotkevich, V. V.; Morozov, S. M.; Geim, A. K. *Proc. Natl. Acad. Sci. U.S.A.* **2005**, *102*, 10451.

DOI: 10.1021/nl504960u
Nano Lett. 2015, 15, 1122−1127

(25) Huber, H. P.; Humer, I.; Hochleitner, M.; Fenner, M.; Moertelmaier, M.; Rankl, C.; Imtiaz, A.; Wallis, T. M.; Tanbakuchi, H.; Hinterdorfer, P.; Kabos, P.; Smoliner, J.; Kopanski, J. J.; Kienberger, F. *J. Appl. Phys.* **2012**, *111*, 014301.
(26) Lai, K.; Kundhikanjana, W.; Kelly, M.; Shen, Z. X. *Rev. Sci. Instrum.* **2008**, *79*, 063704.
(27) Molina-Sánchez, A.; Wirtz, L. *Phys. Rev. B* **2011**, *84*, 155413.
(28) Allain, A.; Kis, A. *ACS Nano* **2014**, *8*, 7180.
(29) This is in contrast to the conventional assumption for 3D semiconductors, where the band-edge DOS is expected to follow a $\sqrt{E}$-dependence over the narrow energy range at the band edge where the energy-momentum dispersion relation can be approximated as parabolic.
(30) Terrones, H.; López-Urías, F.; Terrones, M. *Sci. Rep.* **2013**, *3*, 1549.
(31) Kuc, A.; Zibouche, N.; Heine, T. *Phys. Rev. B* **2011**, *83*, 245213.
(32) Kadantsev, E. S.; Hawrylak, P. *Solid State Commun.* **2012**, *152*, 909.
(33) John, D. L.; Castro, L. C.; Pulfrey, D. L. *J. Appl. Phys.* **2004**, *96*, 5180.
(34) Xia, J.; Chen, F.; Li, J.; Tao, N. *Nat. Nanotechnol.* **2009**, *4*, 505.
(35) Ilani, S.; Donev, L. A. K.; Kindermann, M.; McEuen, P. L. *Nat. Phys.* **2006**, *2*, 687.
(36) Yoon, Y.; Ganapathi, K.; Salahuddin, S. *Nano Lett.* **2011**, *111*, 3768.
(37) Feng, T.; Konar, A.; Xing, H.; Jena, D. *Appl. Phy* **2007**, *91*, 092109.
(38) Gong, C.; Colombo, L.; Wallace, R. M.; Cho, K. *Nano Lett.* **2014**, *14*, 1714.
(39) Sze, S. M.; Ng, K. K. *Physics of Semiconductor Devices*; Wiley: New York, 2007.
(40) Imtiaz, A.; Wallis, T. M.; Lim, S. H.; Tanbakuchi, H.; Huber, H. P.; Hornung, A.; Hinterdorfer, P.; Smoliner, J.; Kienberger, F.; Kabos, P. *J. Appl. Phys.* **2012**, *111*, 093727.
(41) Imtiaz, A.; Wallis, T. M.; Weber, J. C.; Coakley, K. J.; Brubaker, M. D.; Blanchard, P. T.; Bertness, K. A.; Sanford, N. A.; Kabos, P. *Appl. Phys. Lett.* **2014**, *104*, 263107.
(42) Li, Y.; Xu, X. Y.; Zhen, L. *Appl. Phys. Lett.* **2013**, *102*, 143110.

DOI: 10.1021/nl504960u
Nano Lett. 2015, 15, 1122−1127